ACS Catalysis

Research Article

pubs.acs.org/acscatalysis

Electrochemical and In Situ Spectroscopic Evidences toward Empowering Ruthenium-Based Chalcogenides as Solid Acid Fuel Cell Cathodes

Shraboni Ghoshal,[†] Qingying Jia,[†] Jingkun Li,[†] Fernando Campos,[‡] Calum. R.I Chisholm,[‡] and Sanjeev Mukerjee*[,†]

[†]Department of Chemistry, Northeastern University, Boston, Massachusetts 02115, United States

[‡]SAF Cell Inc., 36 South Chester Avenue, Pasadena, California 91106, United States

Supporting Information

ABSTRACT: A low-cost Ru-based chalcogenide catalyst has been used as a cathode catalyst in solid acid fuel cells (SAFC). With sequential addition of Se and Mo on Ru/C in a controlled manner, the resulting physical and electrochemical properties have been discussed in detail. The oxygen reduction reaction (ORR) in the presence of phosphoric acid has been performed to appraise the tolerance of the catalyst in the presence of phosphate anions. Considering the phosphate-rich environment during cell operation, this study is especially relevant for designing catalysts for s. In order to estimate the coverage of phosphate anions on active sites, a semiquantitative analysis of the corresponding Tafel plots has been done. Electrochemical, thermogravimetric, and in situ X-ray absorption spectroscopic experiments have been performed to get a deeper perception of the catalyst−electrolyte interface and account for the high stability of the chalcogenide catalyst at room temperature as well as at elevated temperature. Steady-state polarization curves in SAFC have been collected for over 120 h using the chalcogenide catalyst operating at 250 °C.

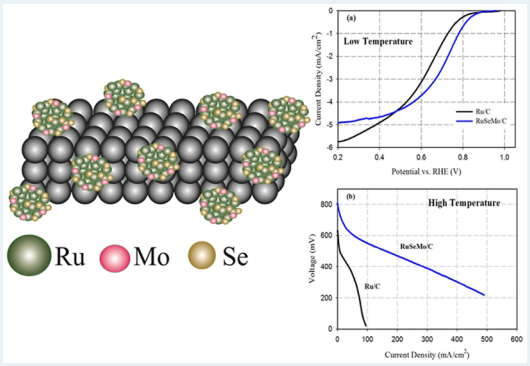

KEYWORDS: *oxygen reduction reaction, electrochemistry, chalcogenides, anion poisoning, X-ray absorption spectroscopy, solid acid fuel cell technology*

1. INTRODUCTION

Establishment of fuel cell technology in electrical power market requires addressing certain concerns, such as high manufacturing cost, demand of ultrapure fuels costs, and cost of precious metal catalysts.[1,2] The majority of these issues can be addressed by employing intermediate temperature fuel cells, which work in the temperature range between 180 and 300 °C.[3] One of the earliest examples, phosphoric acid fuel cells (PAFC), with typical operating temperature between 150 and 200 °C clearly demonstrates the potential advantage of combined heat and power (CHP) with total CHP efficiency in the range of 70% and a concomitant lowering of the balance of plants involved in reforming fuels such as methane, with demonstrated CO tolerances in the range of 1−2%.[4−6] Although this reduces the cost of fuel, phosphoric acid fuel cells have limitations such as prolonged membrane electrode assembly (MEA) preparation, dependence on platinum as anode and cathode catalyst, and inadequate heat cultivation.[7] In fuel cells, the use of higher temperature ceramic proton conductors based on hydrogen-bonded tetrahedral oxyanions in conjunction with a metal cation such as Cs have been introduced in 2004 by Haile et al.,[8,9] as exemplified by cesium dihydrogen phosphate, abbreviated as CDP.[10] Such solid acids like CDP become viable proton conductors after undergoing superprotonic phase transition involving dramatic structural reorientation within the hydrogen-bonded network of the oxyanion moieties, resulting in enhancement of proton conductivity by as much as 4 orders of magnitude.[11] For CDP, this transition initiates at 231 °C, which makes the operating temperature of solid acid fuel cells (SAFC) to be around 250 °C.[12] Such SAFC offer several advantages: (i) SAFC allows relaxation on the purity of the feedstock; (ii) requires simple build up and thus minimizes the radiator size; (iii) Unlike Nafion, CDP exhibits anhydrous proton transport (superprotonic transfer), and hence, fancy humidification system is not required; and lastly, (iv) enables inexpensive stack construction.[13,14] However, the primary concern in enabling SAFC to reach commercial success is the cost associated with the MEA. Also, CDP reacts with a vast number of metal oxides and forms nonconductive phases, thus severely restricting the choice of catalytic materials. Currently, SAFC operation relies mostly on unsupported platinum catalyst, with an average loading of ∼3 mg/cm^2. This translates to 11−25 g of platinum/KW, which is approximately 20 times higher than the loading requirement in PEMFC. Therefore, the

Received: August 23, 2016
Revised: October 28, 2016
Published: December 5, 2016

DOI: 10.1021/acscatal.6b02417
ACS Catal. 2017, 7, 581−591

immediate goal is to significantly reduce the MEA cost by employing cheaper catalysts.

Ongoing efforts toward engendering nonprecious metal electrocatalysts for oxygen reduction reaction (ORR) have resulted in various catalyst configurations, including (a) metal−nitrogen−carbon network (Zelenay et al. and Dodelet et al.),[15−17] (b) transition-metal nitrides/oxynitrides (Ota et al.),[18−21] and (c) transition metal-chalcogen cluster compounds.[22−24] Catalysts of type (a) comprise carbon as the major constituent, with trace amounts of active metals (<5% by weight). These catalysts have appreciable ORR activity comparable to that of Pt/C in acid.[25,26] However, high carbon content restrains the use of these catalysts in SAFC owing to both poor mass transport considerations and carbon corrosion. The transition-metal nitrides (Ota et al.,[18,20,21,27]) mostly based on nitrides and oxy-nitrides of Ta, Nb, and Zr, also suffer from very low density of active sites and relatively lower activity compared to their contemporaries, resulting in poorer ORR activity, even at elevated temperature. Hence, this work is based on examining the choice of semiconducting transition-metal chalcogenides.

Semiconducting, crystalline Chevrel phases (such as $Ru_xMo_{6-x}X_8$) first reported by Alonso Vante et al.,[23,28] have been shown to reduce oxygen both in acid[23] and alkaline environments[29] at low temperatures (ambient). In such catalysts, the transition-metal clusters (Ru) act as reservoirs of electronic charge and form the core of the particle, whereas the chalcogen (X) resides at the periphery coordinated to the Ru core.[30] Ru and chalcogen coexist on the surface of the particle, where Ru serves as the active center for molecular oxygen binding, while X provides protection to Ru against undergoing oxidation.[30] It is believed that the contribution of Mo is mostly to increase the oxygen binding ability of the catalyst, though no fundamental details on this phenomenon are present in literature. In addition to their electrocatalytic activity toward ORR, these catalysts show exceptional endurance when exposed to strongly adsorbing anions such as Cl^- and $H_2PO_4^-$. Such anion resistance has been extensively reported by Ziegelbauer et al.,[31] in the context of HCl recovery process. A report on the application of various chalcogen modified catalysts (using variable constituents and different synthetic routes) in HCl recovery cell has been published, and these catalysts have shown to outperform the state-of-the-art catalysts (e.g., Pt/C and Rh/C).[31] A plenary study on Ru/C with sequential addition of Se and Mo, and their effect on ORR catalysis in alkaline electrolyte has been reported by Ramaswamy et al.,[29,32] where a detailed X-ray absorption spectroscopy (XAS) experiment under in situ conditions has provided information on structure and mechanism of the resulting catalysts in alkaline media.

In this report, we have critically investigated the prospects of Ru-based chalcogenides as potential oxygen electrode in SAFCs. Electrochemical characterizations on Ru/C, RuSe/C, and RuSeMo/C have been performed in acid electrolyte to understand the effect of chalcogen modification on the Ru surface. Surface characterization, ORR catalysis profile, and anion poisoning effect have been combined to delineate the complete profile of the electrocatalysts. In situ XAS experiments at Ru, Se, and Mo edges provide fundamental evidence which help in elucidating the structural and electronic features of the catalysts in acid electrolyte. Through thermogravimetric, electrochemical, and in situ XAS experiments, we have successfully explained the remarkable stability of the chalcogenide catalyst over a wide temperature range. To our knowledge, this is the first time SAFC operation is demonstrated using a cathode catalyst devoid of Pt or Pd. This report also constitutes the highest temperature at which a chalcogen has been shown to function as an ORR electrocatalyst.

2. EXPERIMENTAL SECTION

2.1. Synthesis. The Ru/C, RuSe/C, and RuMoSe/C catalysts were synthesized via a wet chemical reduction method in aqueous medium as described in a prior publication.[29] To synthesize Ru/C, Vulcan XC-72-R carbon and ruthenium chloride were dispersed in water and heated at 80 °C. The slurry was cooled, and alkaline sodium borohydride solution was added as the reducing agent. It was followed by heating the slurry at 80 °C, in order to complete the reduction process. The slurry was then filtered, dried and pyrolyzed at 500 °C for 2 h under argon at a slow heating rate of 4 °C min^{-1}. To synthesize RuSe/C and RuSeMo/C, calculated amounts of selenium oxide and phosphomolybdic acid were added along with ruthenium chloride. A 46.1% Pt/C procured commercially (Tanaka, Japan) was used for comparative studies.

2.2. Physicochemical Characterization. X- ray diffraction characterization was conducted using a Rigaku Ultima IV XRD with Cu Kα source (lambda = 1.541 Å) operated at 40 kV and 44 mA. $2\theta/\theta$ scans were conducted using a 0.05 step size and 5 s hold per step. Scanning electron microscopy (SEM) characterizations were performed using a Hitachi S- 4800 FE-SEM. For validating sample elemental composition, EDAX Genesis on the same SEM instrument was used. Thermogravimetric analysis (TGA) was done using TA Instruments model Q 600. To collect the data, sample was heated until 250 °C under air at a heating ramp rate of 10 °C min^{-1}. The sample was isothermally held at 250 °C for 30 min under air atmosphere, followed by a cool-down procedure to room temperature.

2.3. Electrochemical Characterization. All electrochemical measurements were taken at room temperature using a rotating ring disc electrode (RRDE) from Pine Instruments connected to an Autolab (Ecochemie Inc., model PGSTAT 30) potentiostat/galvanostat. Tests were conducted in a 50 mL jacketed three-electrode cell in 0.1 M $HClO_4$. For each test, freshly made, reversible hydrogen electrode (RHE), was used as the reference electrode with a Pt mesh wire serving as a counter electrode. A glassy carbon disc (geometrical area of 0.247 cm^2) with a gold ring was used as working and ring electrode, respectively. All the results shown here were collected after conditioning the electrodes at a scan rate of 50 mV/s for 50 scans in a voltage range between (0.05−0.8 V), or until stable features were achieved. For Ru-based catalysts, the catalyst loading was maintained at 20 ug/cm^2_{geo}. The gold ring used for ring collection data was held at 1.1 V vs RHE while carrying out the ORR measurements.

2.4. X Ray Absorption Spectroscopy (XAS) Measurements. The in situ synchrotron XAS studies were conducted at the Ru (K-edge, 22117 eV), Se (K-edge, 12658 eV), and Mo (K-edge, 20000 eV) binding energies at SSRL (Stanford Linear Accelerator Center, CA) beamline 2-2. Detailed description of the spectro-electrochemical cell is given in a previous publication from our group.[33] All the data at the Ru K-edge were collected in transmission, while all the Se and Mo K-edge data were collected under fluorescence mode. For transmission data, typically a three-gas ionization detector (I_o, I_t/I_f, and I_{ref})

DOI: 10.1021/acscatal.6b02417
ACS Catal. 2017, 7, 581−591

setup was used with 10% photon absorption in I_0 and 50%−70% in I_t and I_{ref}. The fluorescence detector used was a 13 element Ge detector. Typical loading of the electrode used in these studies were based on the transmitted X-ray absorption cross section designed to provide a step height of unity. Nitrogen saturated 0.1 M $HClO_4$ was used as the electrolyte along with an RHE made out of the same electrolyte. Complete details of EXAFS analysis have been described in detail previously.[29,34] Briefly, IFEFFIT suite 1.2.9 was used for background subtraction using AUTOBK algorithm and normalization. Typical K-range window used was 3−14.0 $Å^{-1}$. The data were processed and fitted using the Athena[35] and Artemis[36] programs. The χ(R) transforms were modeled using single scattering paths calculated by the FEFF6 code.[37] In addition to the bulk averaged EXAFS analysis for obtaining short-range atomic order around Ru (bond distance, coordination number, Debye−Waller factor, etc.), surface-specific information was obtained using a previously developed[38,39] subtractive method referred to as delta mu ($\Delta\mu$) involving the near edge part of the spectrum (X-ray absorption near edge structure, XANES), where the effect of the invariant bulk signal was removed from the surface by subtracting XANES measured at a reference potential (0.1 V vs RHE) from other potentials of interest. Data analysis for delta mu ($\Delta\mu$) studies at Ru K-edge X- ray absorption near-edge structure (XANES) spectra involved specific normalization procedures detailed elsewhere.[29] This involved careful calibration of edge energy (Ru K-edge, 22117 eV) and alignment to the standard reference scan to account for any drift in the beam energy. A post-edge-normalization procedure was then applied to the aligned scans via a cubic spline function, which normalizes the oscillations over a specific energy range (typically 25−200 eV with respect to E_0), thus enabling normalized data on a per-atom basis. Difference spectra were obtained using the equation $\Delta\mu = \mu(V) - \mu(0.1\ V)$, where μ(V) is the XANES at various potentials and μ(0.1 V) is the reference signal at 0.1 V, where Ru surface can be considered to be clean (i.e., free of surface adsorbates). These experimental difference signature profiles were then compared with theoretically generated profiles constructed using cluster models and the FEFF 8.0 code. Detailed modeling of the clusters in the context of surface-adsorbed species was not necessary in this study as the primary focus was to examine the extent of susceptibility toward anion adsorption. Prior studies of such nature have been reported.[40,41]

2.5. MEA Testing in Solid Acid Fuel Cell. *2.5.1. Membrane Electrode Assembly (MEA) Preparation.* For a typical SAFC 3/4 in. button cell, MEAs were made using a standard carbon-supported platinum for anode and RuMoSe/C catalyst as cathode. For the anode side, a nickel mesh was used as a current collector, whereas a stainless steel mesh served as the current collector on the cathode side. The proton conductor was a layer of CDP pressed against the catalyst layers. A nickel mesh, carbon paper, anode catalyst, and the CDP layer were compiled together using a Teflon sheet along the circumference to assemble the half MEA. The cathode catalyst was then mixed with CDP in a ratio of 1:3. Fifty milligrams of this catalyst CDP mixture was taken and spread on the CDP layer. Metallic shims were used to spread the catalyst layer evenly. The full MEA was then pressed under a pressure of 3 t for 3 s. A firm and even spreading of the catalyst layer could be seen after taking it out of the press station. A Teflon tape was used to wrap the MEA along the circumference. This MEA was used for testing in a solid acid fuel cell.

2.5.2. MEA Testing Protocol. MEA was placed inside the test fixture and sealed properly to avoid potential gas leakage. The test fixture was heated in a stepwise manner with different types of gases flows at different stages. In the first step, dry nitrogen gas was purged until 150 °C. Once at 150 °C, humidified nitrogen gas was fed until 250 °C, using a very slow ramp rate. When a stable 250 °C temperature was reached, humidified H_2 and air as feedstocks were introduced to the anode and cathode chambers, respectively. After recording the open circuit voltage (OCV) for 15 min, I−V polarization measurements data were collected. After completion of data collection, cell temperature was gradually reduced, under flowing nitrogen gas, in order to shut down the test station.

3. RESULTS AND DISCUSSION

3.1. Physicochemical Characterizations. Elemental analysis of Ru/C, RuSe/C, and RuMoSe/C were performed using the energy-dispersive spectra (EDS), and the results are listed in Table 1. Representative XRD profiles of Ru/C and RuSe/C collected from 2θ values of 20−80° are shown in Figure 1. The pattern for Ru/C contains distinctive Ru phase with a hexagonal close packed structure ((hcp), space group P63/mmc) with a lattice constant of $a = b = 2.7106$ and $c = 4.2911$, in good agreement with JCPDS powder diffraction pattern. The XRD pattern for RuSe/C shows the presence of the primary peaks of Ru hcp structure, along with peaks corresponding to $RuSe_2$. $RuSe_2$ exists as a pyrite structure with space group $Pa3$ and lattice constants $a = b = c = 5.9297$. Based on Ru (101) crystallite line broadening, the ruthenium crystallite size was estimated to be 8.6 nm for Ru/C and 5.4 nm for RuSe/C, which corroborates that Se atoms reduce the sintering of underlying Ru particles during heat treatment. The comparison of the XRD patterns between Ru/C and RuSe/C reveals that the underlying Ru lattice did not undergo

Table 1. Physicochemical Characterization of Heat-Treated Ru/C, RuSe/C, and RuSeMo/C Catalysts Using EDS

catalyst	Ru (wt %)	Ru:Se:Mo
Ru/C	40%	---
RuSe/C	30%	1:0.5
RuSeMo/C	30%	1:0.5:0.2

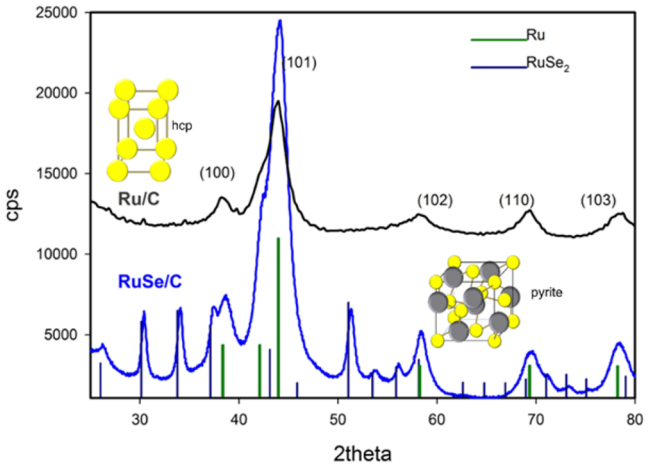

Figure 1. X-ray diffraction pattern of Ru/C and RuSe/C with representative crystal structures.

DOI: 10.1021/acscatal.6b02417
ACS Catal. 2017, 7, 581−591

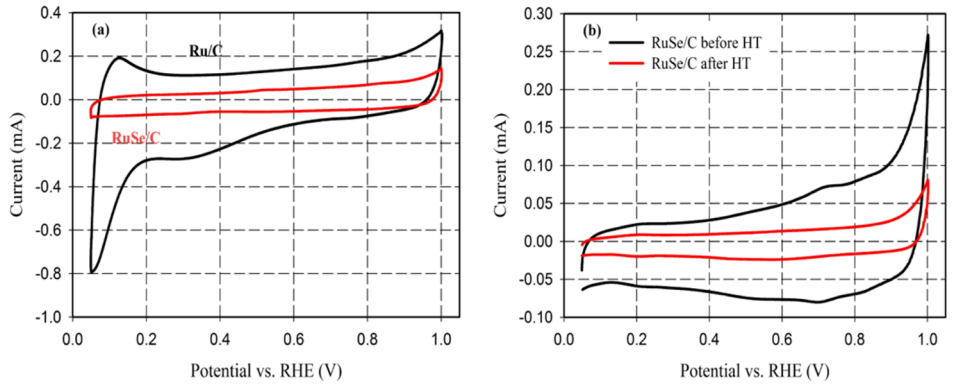

Figure 2. Cyclic voltammetry in deoxygenated 0.1 M $HClO_4$ electrolyte measured at 20 mV/s scan rate of (a) Ru/C(HT) and RuSe/C (HT) catalysts (b) untreated and heat treated RuSe/C catalysts.

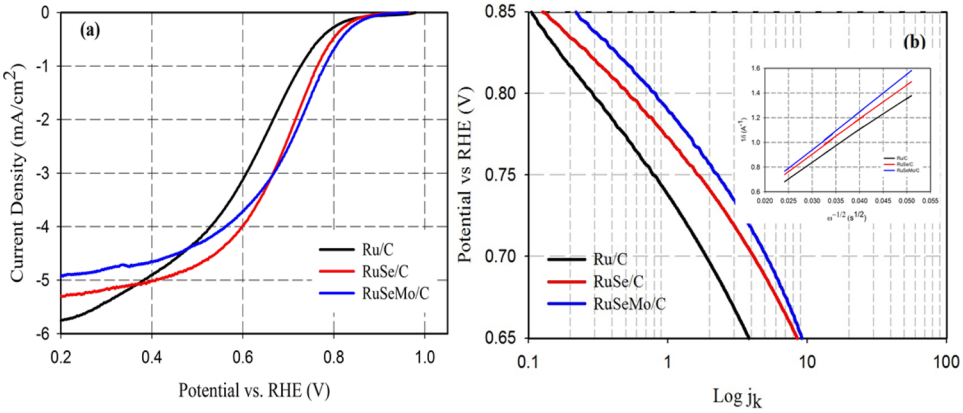

Figure 3. Oxygen reduction reaction on Ru/C, RuSe/C and RuSeMo/C (all heat treated) in O_2- saturated 0.1 M $HClO_4$ electrolyte (a) ORR polarization curves measured at 1600 rpm and 20 mV/s scan rate. (b) Mass transport corrected Tafel plots and (inset) K–L plots.

significant change upon addition of selenium. XRD pattern of RuSeMo/C was similar to that for RuSe/C (not shown here), indicating that Mo does not affect the crystallographic profile of the catalyst.

3.2. ORR on Ru-Based Chalcogenide Catalysts. *3.2.1. Cyclic Voltammetry (CV): Electrochemical Surface Characterization.* Figure 2a compares the CV of Ru/C and RuSe/C catalysts in Ar-saturated 0.1 M $HClO_4$ electrolyte. Ru/C shows a distinctive hydrogen adsorption and desorption peak, which disappears after modifying Ru/C with Se. Such behavior has been reported in other publications as well.[42] Double-layer capacitance decreases following Se addition to Ru/C, which indicates an increase in charge-transfer resistance for both hydride and oxide formation originating from Ru and Se interactions.[43] In Ru/C, an anodic current corresponding to Ru–OH formation and a cathodic current corresponding to the reduction of Ru–OH can be detected. Comparing the CVs of RuSe/C and Ru/C, it is clear that Se modification significantly suppresses Ru–OH formation. Figure 2b shows the effect of heat treatment on RuSe/C. In the untreated sample, the irreversible oxidation peak at 0.83 V in the cyclic voltammogram of Figure 2b indicates oxidation of Se^0 to Se^{4+}. The broad anodic peak from 0.2 V until 1.0 V is due to the combined formation of RuO_2 and SeO_2. However, after heat treatment, there is a single anodic peak at 0.90 V vs RHE corresponding to Se oxidation, thus indicating stabilization of the Ru/C moiety. This observed increase in stability of heat treated RuSe/C is due to an improved alloy formation between the metals, thereby preventing the formation of Se and Ru oxides.[43,44] The CV of RuSeMo/C had similar features as that for RuSe/C, and is shown in the Supporting Information, Figure S1.

3.2.2. ORR Measurement on Chalcogen Modified Ru/C Catalysts. Figure 3a compares the ORR activity profiles of Ru/C, RuSe/C, and RuSeMo/C catalysts in O_2-saturated 0.1 M $HClO_4$ electrolyte recorded at 1600 rpm. The onset of oxygen reduction reaction in Ru/C occurs at 0.81 V vs RHE and ORR is kinetically controlled even at high overpotential, with no defined limiting current region. Addition of Se undeniably improves the ORR activity, with the onset now shifting to 0.85 V vs RHE. The mixed kinetic-diffusion region between 0.8 and 0.5 V is followed by a well-defined limiting current. Chalcogen modification causes a net 86 mV anodic shift in the half-wave potential compared to Ru/C. The effect of the ternary metal molybdenum is self-explanatory in the ORR profile of RuSeMo/C. The onset of ORR for RuSeMo/C happens at 0.86 V, with a positive shift in half-wave potential by 96 mV compared to Ru/C. RuSeMo/C exhibits a mixed kinetic-diffusion current region between 0.86 and 0.5 V, and a prominent limiting current region can be identified. This is in accordance with our previously reported data where similar trends were obtained in alkaline electrolyte.[29] The representative Tafel plots and Koutecky–Levich (K–L) plots are presented in Figure 3b. Tafel slopes of Ru/C, RuSe/C, and RuSeMo/C exhibit similar features with a typical two slopes region. This seems to indicate that the mechanism for ORR most likely does not change on chalcogen modification or ternary Mo addition. Detailed Tafel slope analysis however was not possible as they are not amenable on supported catalysts.

DOI: 10.1021/acscatal.6b02417
ACS Catal. 2017, 7, 581–591

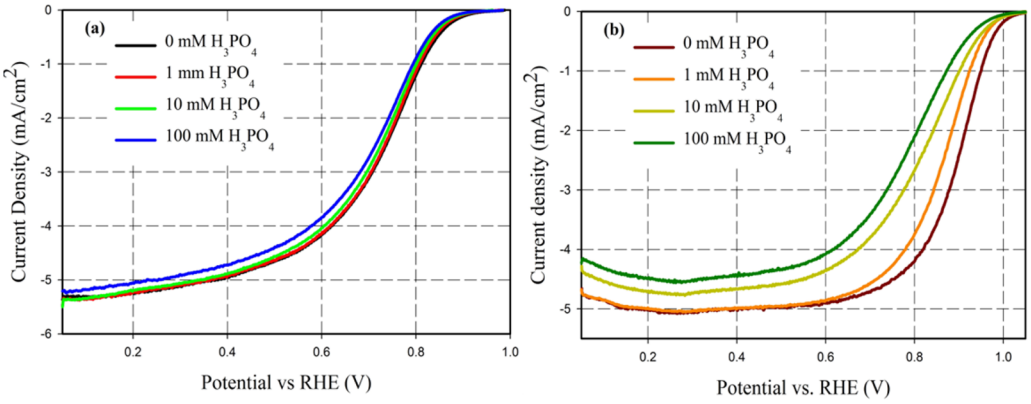

Figure 4. Phosphate poisoning study in O_2-saturated 0.1 M $HClO_4$ measured at 1600 rpm and 20 mV/s scan rate on (a) RuSeMo/C and (b) Pt/C.

Table 2. Effect of Phosphoric Acid Doping on the ORR Performances of Pt/C and RuSeMo/C Catalysts in O_2-Saturated 0.1M $HClO_4$ Electrolyte Measured at 1600 rpm and 20 mV/s Scan Rate

catalyst	concn of H_3PO_4 (mM)	number of transferred electrons (n)	$E_{1/2}$ (V)	Tafel slopes (mV/dec)	Δ (mV/dec)	Φ
Pt/C	0	4.00	0.893	159/60	99	1
	1	4.00	0.864	144/61	83	1.16
	10	3.92	0.818	160/76	84	1.16
	100	3.87	0.792	154/75	79	1.26
RuSeMo/C	0	3.5	0.725	143/81	62	1
	1	3.5	0.721	139/75	64	0.97
	10	3.45	0.718	137/63	63	0.98
	100	3.43	0.707	134/73	61	1.01

Assessment of the K−L plots provided further insight into the effect of chalcogen modification on Ru/C. The theoretical Levich slope was calculated using the following parameters: Diffusivity (D_{O_2}) = 1.9 × 10^{-5} cm^2/s, solubility (C_{O_2}) = 1.18 × 10^{-6} mol/cm^3, and kinematic viscosity (ν) = 8.93 × 10^{-3} cm^2/s. The number of electrons transferred on Ru/C was determined to be 2.95, which increased to 3.17 on addition of Se. In RuSeMo/C, K−L plot analysis showed the number of transferred electrons to be 3.5. This supports the theory of peroxide spillover by Mo, which aids in shifting the ORR pathway toward the more efficient four-electron route. Similar conclusion on the role of Mo was reported by Alonso Vante et al. in their studies on the effect of Mo on the ORR profiles of Ru/Se systems.[45] The respective ring current response has been shown in the Supporting Information (Figure S2) to get an illustrative idea on the H_2O_2 generation, along with the results obtained from RRDE experiments as reported in Table S1. It is intriguing to note how the ORR pathway shifts from a two-electron route for unmodified Ru/C toward a four-electron route in Se and Mo modified Ru/C. Vante et al.[46] have explained this in terms of the binding mode of O_2 on Ru surface in the different catalysts. While unmodified Ru/C gets passivated easily, the number of Ru active sites are greatly reduced. This prompts the oxygen molecule to bind in a terminal mode, which directs ORR to a two-electron reduction pathway to H_2O_2. On the other hand, Se modification helps to preserve the Ru active sites by preventing them from getting oxidized. This leads to a 2-fold binding of oxygen on Ru surface, thus ensuring dissociative adsorption of O_2 leading to four-electron reduction. All the above results unequivocally imply that modification of Ru/C catalyst with Se and Mo is crucial when implementing Ru-based system as ORR electrocatalyst in a fuel cell. However, considering the phosphate-rich electrolyte in SAFC, it is important to ascertain that RuSeMo/C is resistant to phosphate anion poisoning. Therefore, the calculated amount of phosphoric acid was doped into 0.1 M $HClO_4$ electrolyte, and corresponding ORR polarization curves for RuSeMo/C were collected.

3.2.3. Effect of H_3PO_4 Addition on ORR Performance for RuMoSe/C. The presence of phosphates in CDP can potentially restrain catalytic activity of the oxygen electrode in a SAFC. Phosphate anions have strong affinity toward platinum, thereby resulting in significant poisoning of active sites at concentrations as low as 0.1 mM.[47] In order to examine the tolerance of the chalcogenide catalyst in the presence of phosphate ions, oxygen-saturated 0.1 M $HClO_4$ electrolyte was doped with a calculated amount of phosphoric acid. Figure 4a,b show the ORR profile of both Pt/C and RuMoSe/C in the presence of phosphate ions, where Pt/C catalyst is used as control. Both the catalysts exhibit three characteristic potential regions: a diffusion controlled region (<0.4 V for RuMoSe/C and <0.7 V for Pt/C), mixed diffusion−kinetic limitation region (0.45 V to 0.75 V for RuMoSe/C and 0.65 V to 0.85 V for Pt/C), and a Tafel region (>0.8 V for RuMoSe/C and >0.9 V for Pt/C). For both the catalysts, the half-wave potential ($E_{1/2}$) shifts cathodically with increasing concentration of H_3PO_4. The $E_{1/2}$ values at different concentrations of H_3PO_4 are shown in Table 2. Interestingly, for RuMoSe/C, the overall shift in $E_{1/2}$ value amounted to 18 mV in the concentration range of 0 mM to 100 mM H_3PO_4, whereas for the same concentration range of H_3PO_4, a net shift of 100 mV in $E_{1/2}$ value occurred for Pt/C. Assuming the concentration of O_2 does not change while adding the aliquots of H_3PO_4, the number of exchanged electrons were calculated using the K−L equation. In Pt/C, n decreases from 4.00 (at 0 mM H_3PO_4) to 3.87 at 100 mM H_3PO_4 concentration whereas for RuSeMo/C, n drops from 3.50 (at 0 mM H_3PO_4) to 3.43 at 100 mM H_3PO_4 concentration. These results clearly show that compared to

DOI: 10.1021/acscatal.6b02417
ACS Catal. 2017, 7, 581−591

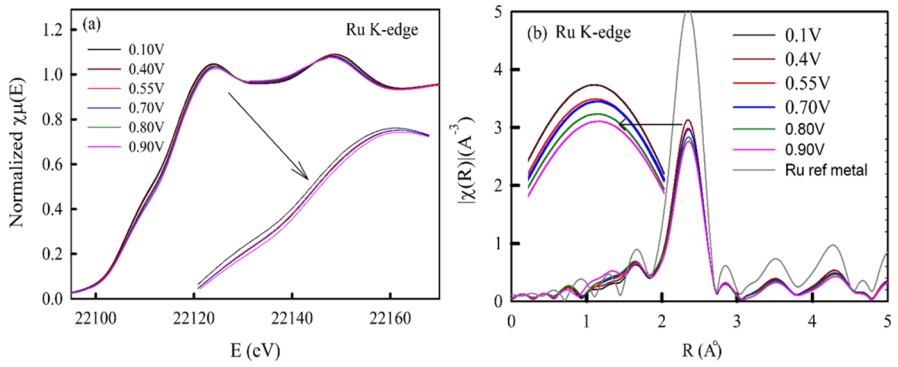

Figure 5. In situ XANES (a) and FT- EXAFS (b) of Ru/C (HT) catalyst in Ar-saturated 0.1 M $HClO_4$ electrolyte at Ru K-edge.

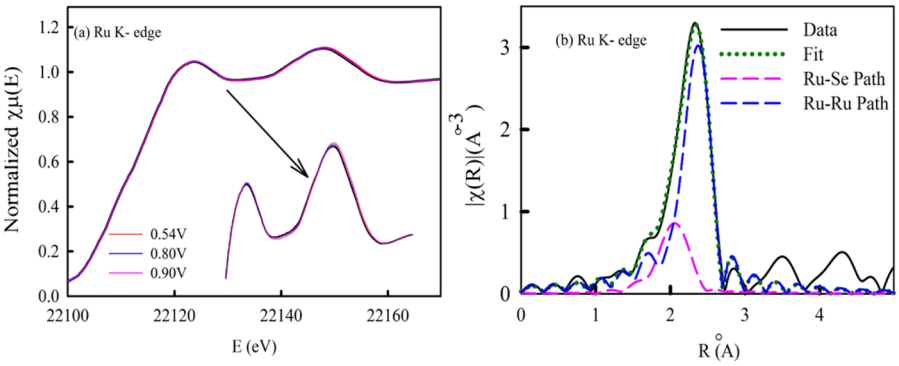

Figure 6. In situ (a) XANES and (b) FT-EXAFS of RuSeMo/C (HT) catalyst collected in deaerated, Ar-saturated 0.1 M $HClO_4$ electrolyte at Ru K-edge.

Pt/C, phosphate adsorption is significantly suppressed on the chalcogenide catalyst.

Park et al.[48] studied the effect of phosphoric acid on Se-modified Ru/systems and reported enhancement of ORR activity. They ascribed adsorption of phosphate anion on Se atoms and lower O_{ads} on Ru atoms as a possible reason functioning via a combination of steric and electrostatic repulsions. Our results, however, did not show any enhancement in ORR activity, but the effect on onset potential, limiting current, or half-wave potential is minimal as compared to Pt/C.[48] Analysis of the mass-transport-corrected Tafel plots can give an estimation of the coverage of phosphate anions on an electrocatalyst surface. Assuming that ORR reaction is first-order with respect to O_2 concentration, the Tafel curves are derived as

$$E = E_0 + b \log \frac{j}{j_0}$$

where E_0 = 1.23 V vs RHE under standard conditions, b is Tafel slope, j_0 is exchange current density, and j_k is the kinetic current density. Typically, two different Tafel slopes are ascribed to difference in the extent of oxide coverage on the catalyst surface in low and high current densities. He et al.[47,49] have utilized this trend of Tafel slopes to correlate effects of oxide formation versus those arising from effects of oxide formation along with $H_2PO_4^-$ adsorption. Values of Δ and Φ can determine the extent of $H_2PO_4^-$ adsorption, in a semiquantitative manner, where Δ and Φ can be defined as

$$\Delta = t_h - t_l$$

$$\Phi = \Delta_{M0}/\Delta_M$$

where t_h and t_l are the Tafel slopes in high and low current density regions, Δ_{M0} and Δ_M are the Δ values in 0.1 M $HClO_4$, without and with H_3PO_4 doping, respectively. A lower Δ_M results in higher Φ, which is indicative of $H_2PO_4^-$ adsorption interfering with oxide formation. As seen in the table, Φ increases rapidly for Pt/C, whereas it remains mostly constant for RuMoSe/C. These calculations unanimously support the RDE experimental results and validate the higher tolerance of the chalcogenide catalyst against phosphate poisoning. Doping experiments were performed using cesium dihydrogen phosphate, and similar results were obtained (Figure S3).

3.3. In Situ XAS Experiment. XAS measurements were carried out under in situ electrochemical conditions in 0.1 M $HClO_4$ at the K-edges of Ru, Se, and Mo on the RuSeMo/C catalyst, as well as on the Ru/C catalyst for comparisons. It should be noted that the XAS was conducted at room temperature, whereas the SAFC cell operates at ∼250 °C. Despite this, it is reasonable to assume that structure of the catalysts does not change drastically within this relatively low temperature range, especially the structural difference existing between the Ru/C and RuSeMo/C. This is manifested in the stable thermal behavior (up to 250 °C) observed using DSC/TGA reported in the supplementary section. Therefore, the in situ XAS, in combination with ex situ characterization results given above, can provide valuable information on the structural and electronic properties of the catalysts as shown.

Figure 5a shows the XANES spectra obtained at the Ru K-edge on the Ru/C−HT catalyst in Ar-saturated 0.1 M $HClO_4$ electrolyte at various potentials; the corresponding Fourier transformed (FT) EXAFS spectra are displayed in Figure 5b. The highlighted region in Figure 5a shows the anodic shift of the XANES with increasing potentials, indicating the increase in

DOI: 10.1021/acscatal.6b02417
ACS Catal. 2017, 7, 581−591

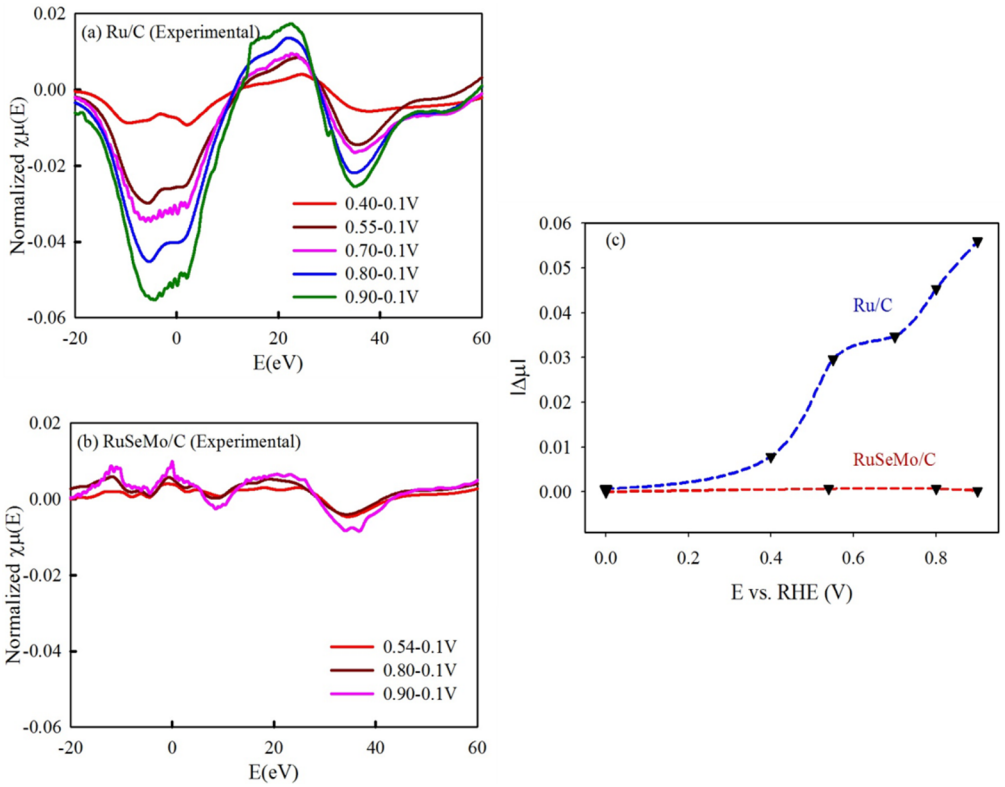

Figure 7. $\Delta\mu$ signatutes using XANES Ru K-edge for (a) Ru/C (HT) catalyst and (b) RuSeMo/C (HT) catalysts (scale is same as in panel (a) to compare the $\Delta\mu$ amplitudes). (c) Plot showing variation of $\Delta\mu$ amplitude as a function of applied potential for Ru/C (HT) and RuSeMo/C (HT) catalysts. Data were collected in Ar-saturated 0.1 M $HClO_4$ electrolytes.

Ru oxidation state with increasing potentials. Concomitantly, the FT-EXAFS peak at 2.5 Å gradually decreases with increasing potential; due to gradual insertion of oxygen atoms into the Ru lattice blocking the Ru−Ru scattering. In sharp contrast to Ru/C, the XANES spectrum for RuSeMo/C at the Ru K-edge does not change with increasing potentials going from 0.1 to 0.9 V (Figure 6a), thereby indicating that the oxidation state of Ru practically remains unchanged within the investigated potential window.

The extent in adsorption of oxygen onto Ru surfaces at elevated potentials is probed by the surface-sensitive $\Delta\mu$ analysis as displayed in Figure 7a. The ascending $\Delta\mu$ amplitude with increasing potentials indicates that the Ru sites are progressively occupied by oxygen adsorbates with increasing potentials. This trend is expected, given the strong oxophilic character of Ru which causes formation of surface oxides at even low potentials. Therefore, a large fraction of the Ru active sites starts to get poisoned by oxygen species at relatively low potentials, and this site-blocking effect limits the catalytic performance of the Ru/C catalysts. In contrast, the corresponding $\Delta\mu$ signals for RuSeMo/C catalyst are minimal (Figure 7b). This indicates that the oxidation of Ru does not occur until 0.9 V. The significant delay of the Ru oxidation in RuSeMo/C catalyst compared to Ru/C greatly alleviates the site-blocking effect and hereby accounts partially for the enhanced ORR activity. Figure 7c explicitly brings out the oxygen coverage difference represented by $\Delta\mu$ amplitude as a function of applied potential in the surface Ru in Ru/C and RuSeMo/C. In addition, the delay of the Ru oxidation until potential beyond 0.9 V reflects the weakening of the Ru−O binding energy, which may also improve the ORR activity given that the binding energy between the Ru/C and oxygen is overly strong.[50]

To unravel the structural origin of the suppression of the Ru oxidation or the weakening of the Ru−O binding energy in the RuSeMo/C catalyst, EXAFS fitting analysis were conducted at the Ru- and Se K-edge simultaneously. The fitting results are listed in Table 3. As shown, the Ru−Ru coordination number (N_{Ru-Ru}) is much higher than the Ru−Se coordination number (N_{Ru-Se}), and the Se−Ru coordination number (N_{Se-Ru}) is also moderately higher than the Se−Se coordination number (N_{Se-Se}). These results indicate that Ru and Se are surrounded mostly by Ru atoms. In addition, while the total coordination number of Ru (N_{Ru-Ru} + N_{Ru-Se}) in RuSeMo/C is slightly

Table 3. In Situ EXAFS Fit Results for RuSeMo/C−HT catalyst Obtained from Experiments Performed at the Ru K-Edge and Se K-Edge as a Function of Potential in Ar-Saturated 0.1M $HClO_4$ Electrolyte[a]

catalyst	Ru/C		RuSeMo/C	
parameters	*N*	*R* (Å)	*N*	*R* (Å)
Ru−Ru	9.2(1.2)	2.66(3)	7.8(6)	2.69(1)
Ru−Se	---	---	1.9(2)	2.44(1)
Se−Ru	---	---	2.1(1.0)	2.44(1)
Se−Se	---	---	0.5(1.0)	2.52(5)

[a] S_0^2 fixed at 0.88 and 0.945 for Ru and Se, respectively, as obtained by fitting the reference foils. Fits were done in *R*-space, $k^{1,2,3}$ weighting. For Ru, 1.23 < *R* < 3.00 Å and Δk = 3.153−13.954 $Å^{-1}$ were used; for Se, 1.369< *R* < 2.802 Å and Δk = 2.794−13.134 $Å^{-1}$ were used. Values in parentheses represent the largest statistical errors of all of the least-squares fits determined by ARTEMIS.

DOI: 10.1021/acscatal.6b02417
ACS Catal. 2017, 7, 581−591

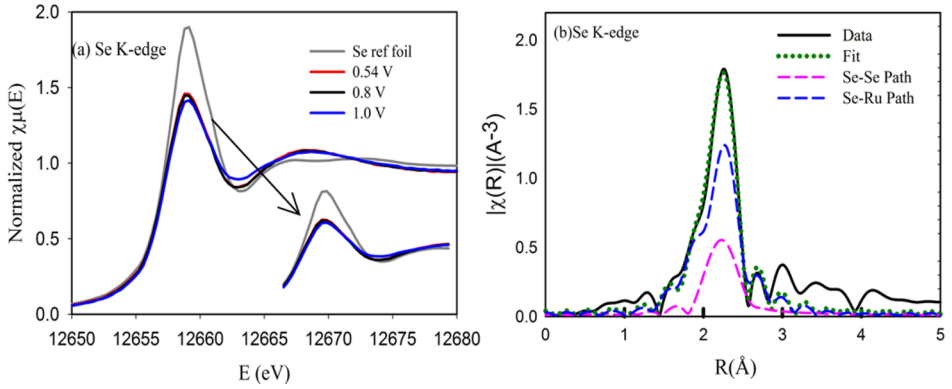

Figure 8. In situ (a) XANES and (b) FT- EXAFS of RuSeMo/C (HT) catalyst in deaerated Ar-saturated 0.1 M $HClO_4$ electrolyte at Se K-edge.

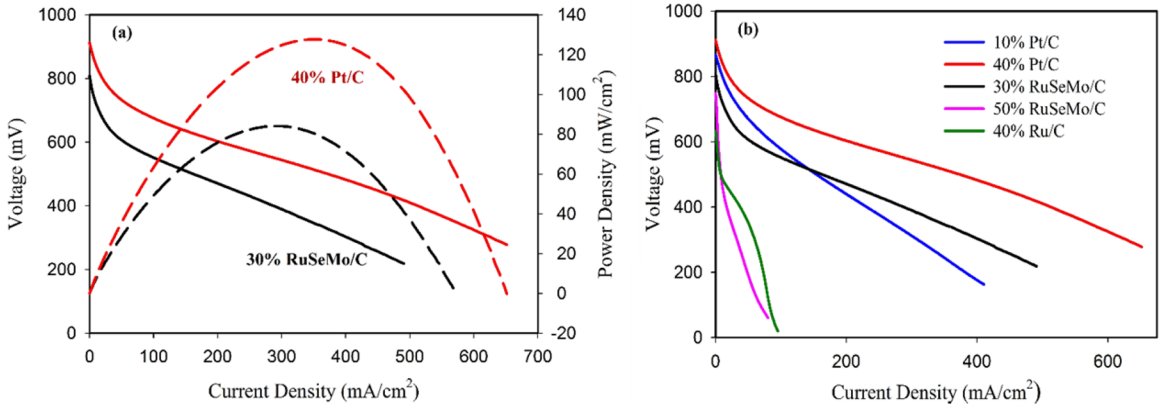

Figure 9. *iR*-corrected SAFC test results collected in H_2 and air, under ambient pressure at a cell temperature of 250 °C. (a) Comparison of 40% Pt/C and 30% RuSeMo/C catalysts—polarization curves and corresponding power density curves. Loading of Pt = 1.8 mg/cm^2; loading of Ru = 1.2 mg/cm^2. (b) Polarization curves obtained from Pt/C- and Ru-based catalysts with various metal loadings.

higher than that in Ru/C, the coordination number of Se (N_{Se-Ru} + N_{Se-Se}) in RuSeMo/C is extremely low. This shows that most of the Se atoms are significantly undercoordinated. Compiling these results together, it can be deduced that the Se atoms are dispersed at the edges and/or corners (undercoordinated positions) of the RuSeMo/C nanoparticles. According to the particle-size effect, the undercoordinated metal atoms in the edges/corners are more vulnerable to oxygen adsorption compared to the atoms in intact facets (such as (111), (100)) because of the stronger binding energy with oxygen.[50] Despite this, Se atoms are not oxidized until 0.8 V as evidenced by the unchanged Se K-edge XANES up to 0.8 V (Figure 8a). The intensity of XANES gets slightly reduced at 1.0 V, which can be ascribed to the insertion of the oxygen atoms into the NPs that reduces the Se−Se/Ru scattering. Such tolerance against oxidation can be explained by looking at the higher electron affinity of Se compared to Ru, making the latter more vulnerable for oxidation. Therefore, the suppression of the Ru oxidation for the RuSeMo/C catalyst is partially ascribed to the replacements of the vulnerable Ru atoms in the edges/corners with oxidation-tolerant Se atoms.

The high N_{Se-Ru} given by EXAFS fitting results given in Table 3 directly shows the interaction between the Ru and Se. Given that the electron affinities between the two elements are drastically different, the ligand effect induced by the charge transfer between them is expected. Indeed, the white line intensity of Se in the RuSeMo/C catalyst is much less than that of Se bulk metal (Figure 8a), which indicates a substantial charge transfer from Ru to Se as expected from their electron affinity values. Accordingly, the Ru XANES of the RuSeMo/C catalyst is also different from that in Ru/C, indicating modifications in the electronic configuration by the ligand effect; however, the difference is less intense compared to Se because Ru is still mostly surrounded by Ru atoms, and the ligand effect is therefore relatively weak. The deficient charge of Ru caused by the charge transfer from Ru to Se hinders the charge transfer from Ru to O, thereby suppressing oxygen adsorption. This was also observed by Babu et al. on Ru/Se systems using EC-NMR and XPS studies.[51]

In addition to the favorable ligand effect induced by Se, compressive-strain effects induced by the insertion of Se is also expected given that the radius of Se is much smaller than that of Ru. Indeed, the Ru−Se bond distance (2.44 Å) in the RuSeMo/C catalyst is much less than the Ru−Ru bond distance (2.69 Å). On the other hand, the Se−Se bond distance (2.52 Å) and Se−Ru bond distance (2.44 Å) are significantly longer than that of the Se reference foil fitted with the same parameters (2.36 Å) (Figure S5). According to the d-band theory developed by Norskov et al.,[52] the compressive-strain weakens the Ru−O binding energy via downshift of the Ru d-band relative to the Fermi level, thereby suppressing the Ru oxidation.

Overall, the subdued Ru oxidation can be attributed to the favorable strain and ligand induced by the decoration of the Se atoms onto the edges/corners of the RuSeMo/C NPs. It should be noted that the FT-EXAFS of both Se and Ru K-edge data can be well-fitted without including the scattering from the Mo neighbors. In addition, the Mo K-edge spectra do not change

DOI: 10.1021/acscatal.6b02417
ACS Catal. 2017, 7, 581−591

Table 4. Comparison between RDE Experimental Results (in 0.1M $HClO_4$ Electrolyte) Toward ORR and Solid Acid Fuel Cell Performance Results As Obtained from 30% RuSeMo/C and 50% RuSeMo/C

		RDE experiment results		SAFC test results	
catalyst	atomic ratio (Ru:Se:Mo)	ORR onset (V)	$E_{1/2}$ (V)	take-off voltage (V)	voltage @ 200 mA/cm^2 (V)
30% RuSeMo/C	1:0.5:**0.2**	0.86	0.623	0.82	0.479
50% RuSeMo/C	1:0.5:**0.4**	0.90	0.743	0.76	---

with applied potentials. These results suggest that Mo does not actively participate in electrocatalysis; this is in congruence with the previous results reported by Ramaswamy et al.,[29] in an analogous system studied in alkaline media. Mo mainly contributes in spilling over peroxide intermediates as shown in the Levich analysis of RuSeMo/C catalyst. This, however, cannot be directly observed by in situ XAS.

3.4. Solid Acid Fuel Cell Testing. Figure 9a demonstrates the steady-state polarization result and corresponding power density curves obtained using 30% RuSeMo/C and 40% Pt/C, in a solid acid fuel cell. In general, small leaks across the cell, microcracks in the electrolyte, and electrolyte resistance mostly account for the performance losses in a solid acid fuel cell. SAFC electrodes requires high CDP to catalyst ratio to sustain optimum protonic conductivity, thus introducing additional performance losses. Moreover, the interaction between CDP and the catalyst plays a vital role in determining the ohmic losses. CDP lacks the ability to percolate the catalyst as much as conventional electrolytes such as Nafion. As a result, both Pt/C and RuSeMo/C catalyst are subjected to substantial losses in the activation region. A standard state of the art 40% Pt/C generates 100 mA/cm^2 current density at 669 $mV_{iR\ free}$, whereas the chalcogenide catalyst executes the same current density at 552 $mV_{iR\ free}$. The chalcogenide catalyst reaches 67% the power density of the standard Pt/C cathode run under the same conditions. When subjected to long time operation, the chalcogenide catalyst exhibits remarkable stability along with a gradual improvement in the performance from beginning of life (BOL) until 120 h (Figure S6).

Metal loading and carbon content play a pivotal role in determining the catalyst performance in a single cell. It is intuitive that a lower carbon content and higher active metal loading in a catalyst will result in superior performance. This in fact, holds true for Pt/C catalyst. As shown in Figure 9b, a 10% Pt/C catalyst can be seen to be losing performance rapidly as compared to 40% Pt/C. Factors such as low platinum content and aggravated carbon corrosion in 10% Pt/C lead to such low-grade performance. However, remarkably different trends are obtained when chalcogenide catalysts with higher Ru loading are tested. Table 4 compares the performances of 50% RuSeMo/C and 30% RuSeMo/C in RDE experiment in 0.1 M $HClO_4$ at room temperature and under SAFC operating conditions. Under RDE experimental conditions, 50% RuSeMo/C has an ORR onset value of 900 mV, compared to 30% RuSeMo/C with an onset at 860 mV (Figure S4). This enhanced performance arises from a higher loading of the ORR active Ru metal in 50% RuSeMo/C resulting in more abundant ORR active sites. Compared to 30% RuSeMo/C, 50% RuSeMo/C shows a positive shift of 120 mV in half-wave potential, with the latter having a well-defined limiting current region at 0.6 V vs RHE as shown in Figure S4. However, SAFC polarization results give an inverse trend. While both 30% RuMoSe/C and 50% RuSeMo/C exhibit a takeoff voltage of 820 mV, the latter catalyst dramatically loses performance and fails to generate current beyond 80 mA/cm^2. A higher metal loading may ensure significant enhancement in performance under RDE experimental conditions, but the SAFC environment is exceedingly different. Other negating factors such as reactivity profile of CDP may become prominent and show a detrimental effect on the catalytic performance. Numerous metals oxides, including Ru and Mo, tend to react with CDP and form nonconducting phases—a phenomenon that is prevalent with SAFC operation. Therefore, a higher loading of Ru and Mo in 50% RuSeMo/C is the most plausible cause for the poor performance of the chalcogenide catalyst, suggesting that an optimum balance of Ru and Mo is crucial for SAFC application.

As a control experiment, unmodified 40% Ru/C catalyst was tested in SAFC. As displayed in Figure 9b, the polarization trend is analogous to that of 50% RuSeMo/C, further indicating that a higher ruthenium content is detrimental to the catalytic performance in the presence of CDP. The disparate features present in the polarization curve for Ru/C as compared to a conventional polarization curve are probably due to the spontaneous reaction occurring between Ru and CDP. Thus, Se modification not only impedes the oxidation of active metal, but also acts as a protective shield against CDP and arrests any possible reaction with Ru. TGA data further establishes the importance of Se modification on Ru/C at high temperature (Figure S7). While Ru/C rapidly loses catalyst weight when held at 250 °C in air, RuSe/C and RuSeMo/C show no such loss. This happens because in the absence of Se, Ru is subjected to oxidation, which makes the Ru moieties electron deficient. This results in rapid carbon corrosion, hence the observed catalytic weight loss. However, in the presence of Se, which has ideal electronegativity, Ru oxidation is significantly mitigated, and optimum electron density in Ru is restored. As a result, no catalytic weight loss occurs in the case of RuSe/C and RuSeMo/C. The slight increase in catalyst weight for the modified catalysts can be due to traces of oxide formation.

4. CONCLUSIONS

In this report, we have critically examined the prospects of RuSeMo/C as cathode catalyst in SAFC, supported by a complete structural and electrochemical characterization. Combined XRD and XAS results prove that chalcogenide catalyst exists as a Ru core with Se atoms residing at the periphery within the Ru lattice. In situ XAS experiment validates the stability of Ru in 0.1 M $HClO_4$ electrolyte beyond 0.9 V, which is essential for fuel cell application. Chalcogen modification plays a pivotal role in the success of RuSeMo/C catalyst in three ways: (i) Se located at the undercoordinated sites suppresses Ru oxidation by inducing ligand and strain effects. Hence, the ORR active Ru sites are well-preserved. (ii) Because Se modification restricts formation of RuO, CDP does not react to form non-conducting phases. This helps to sustain the activity of the catalyst over prolonged hours of operation. (iii) Under a harsh oxidizing atmosphere at 250 °C, Se protects Ru/C from corrosion, which otherwise fails to survive and loses catalytic weight due to carbon oxidation, which is explicitly

DOI: 10.1021/acscatal.6b02417
ACS Catal. 2017, 7, 581−591

proven by TGA results. Ternary metal molybdenum mostly acts toward shifting the ORR pathway toward the four-electron route, which is proven by K−L plot analysis. Compared to Pt/C, the RuMoSe/C catalyst shows higher tolerance toward phosphate anion poisoning. Semiquantitative analyses of the Tafel slopes indicate that phosphate ions alter the platinum surface due to strong adsorption, a phenomenon which is much alleviated in RuMoSe/C. For the first time, SAFC operation using the Ru-based catalyst is reported, and steady-state polarization curves are collected. Although the activity of the chalcogenide catalyst is inferior to Pt/C, the chalcogenide catalyst displays high stability under continuous operation. Furthermore, Ru is considerably cheaper compared to Pt, establishing Ru-based chalcogenides as impressive candidates for SAFC.

Because SAFC is a recent discovery, there are voids in the technology that need to be addressed. Further research on the interaction of CDP with catalysts can give crucial information about predicting catalyst behavior in SAFC. Intensive analytical tools such as in situ Raman spectroscopy and in situ X-ray crystallography may be employed to understand the interaction of superprotonic CDP and catalyst at 250 °C, which will eventually help us to build improvised catalyst models for SAFC.

■ ASSOCIATED CONTENT

Supporting Information

The Supporting Information is available free of charge on the ACS Publications website at DOI: 10.1021/acscatal.6b02417.

Additional experimental results on RDE, RRDE, TGA, and XAS experiments (PDF)

■ AUTHOR INFORMATION

Corresponding Author

*E-mail: s.mukerjee@neu.edu. Tel.: 617-373-2382. Fax: 617-373-8949.

Notes

The authors declare no competing financial interest.

■ ACKNOWLEDGMENTS

The authors deeply appreciate the financial support from U.S Department of Energy funded ARPA−ENERGY (Award number DE-FOA-0001026). The authors would like to thank Stanford linear Accelerator Center for allowing them to work at the Stanford Synchrotron Radiation Laboratory and perform the X-ray absorption experiments. Use of synchrotron facilities were supported by the U.S. Department of Energy, Office of Science, Office of Basic Energy Sciences, former under the Contract No. DE-SC0012704 and DE-AC02-76SF00515, respectively. The valuable assistance of Dr. Syed Khalid and Dr. Nebojsa Marinkovic (beam 2-2, SSRL) is gratefully appreciated.

■ REFERENCES

(1) Debe, M. K. *Nature* **2012**, *486*, 43−51.
(2) Gasteiger, H. A.; Kocha, S. S.; Sompalli, B.; Wagner, F. T. *Appl. Catal., B* **2005**, *56*, 9−35.
(3) Kunz, H. R. *J. Electrochem. Soc.* **1977**, *124*, C137−C137.
(4) Macdonald, J.; Stonehart, P.; Baris, J. *J. Electrochem. Soc.* **1980**, *127*, C342−C342.
(5) McBreen, J.; Olender, H.; Srinivasan, S.; Kordesch, K. V. *J. Appl. Electrochem.* **1981**, *11*, 787−796.
(6) Xiao, G.; Li, Q. F.; Hjuler, H. A.; Bjerrum, N. J. *J. Electrochem. Soc.* **1995**, *142*, 2890−2893.
(7) He, Q.; Mukerjee, S.; Zeis, R.; Parres-Esclapez, S.; Illan-Gomez, M. J.; Bueno-Lopez, A. *Appl. Catal., A* **2010**, *381*, 54−65.
(8) Haile, S. M.; Boysen, D. A.; Chisholm, C. R. I.; Merle, R. B. *Nature* **2001**, *410*, 910−913.
(9) Boysen, D. A.; Uda, T.; Chisholm, C. R. I.; Haile, S. M. *Science* **2004**, *303*, 68−70.
(10) Boysen, D. A.; Haile, S. M.; Liu, H. J.; Secco, R. A. *Chem. Mater.* **2003**, *15*, 727−736.
(11) Botez, C. E.; Hermosillo, J. D.; Zhang, J. Z.; Qian, J.; Zhao, Y. S.; Majzlan, J.; Chianelli, R. R.; Pantea, C. *J. Chem. Phys.* **2007**, *127*, 194701.
(12) Haile, S. M.; Chisholm, C. R.; Sasaki, K.; Boysen, D. A.; Uda, T. *Faraday Discuss.* **2007**, *134*, 17−39.
(13) Uda, T.; Haile, S. M. *Electrochem. Solid-State Lett.* **2005**, *8*, A245−A246.
(14) Kiho, M.; Matsunaga, K.; Morikawa, S.; Kato, O. *Electrochemistry* **2001**, *69*, 580−586.
(15) Lefevre, M.; Proietti, E.; Jaouen, F.; Dodelet, J. P. *Science* **2009**, *324*, 71−74.
(16) Proietti, E.; Jaouen, F.; Lefevre, M.; Larouche, N.; Tian, J.; Herranz, J.; Dodelet, J. P. *Nat. Commun.* **2011**, *2*, Article No. 416.
(17) Jaouen, F.; Proietti, E.; Lefevre, M.; Chenitz, R.; Dodelet, J. P.; Wu, G.; Chung, H. T.; Johnston, C. M.; Zelenay, P. *Energy Environ. Sci.* **2011**, *4*, 114−130.
(18) Kim, J. H.; Ishihara, A.; Mitsushima, S.; Kamiya, N.; Ota, K. I. *Electrochim. Acta* **2007**, *52*, 2492−2497.
(19) Nam, K. D.; Ishihara, A.; Matsuzawa, K.; Mitsushima, S.; Ota, K.; Matsumoto, M.; Imai, H. *Electrochim. Acta* **2010**, *55*, 7290−7297.
(20) Maekawa, Y.; Ishihara, A.; Kim, J. H.; Mitsushima, S.; Ota, K. I. *Electrochem. Solid-State Lett.* **2008**, *11*, B109−B112.
(21) Liu, Y.; Ishihara, A.; Mitsushima, S.; Kamiya, N.; Ota, K. *Electrochem. Solid-State Lett.* **2005**, *8*, A400−A402.
(22) Fischer, C.; Alonsovante, N.; Fiechter, S.; Tributsch, H. *J. Appl. Electrochem.* **1995**, *25*, 1004−1008.
(23) Vante, N. A.; Jaegermann, W.; Tributsch, H.; Honle, W.; Yvon, K. *J. Am. Chem. Soc.* **1987**, *109*, 3251−3257.
(24) Inukai, J. J.; Cao, D. X.; Wieckowski, A.; Chang, K. C.; Menzel, A.; Komanicky, V.; You, H. *J. Phys. Chem. C* **2007**, *111*, 16889−16894.
(25) Li, J.; Ghoshal, S.; Liang, W.; Sougrati, M. T.; Jaouen, F.; Halevi, B.; McKinney, S.; McCool, G.; Ma, C.; Yuan, X.; Ma, Z. F.; Mukerjee, S.; Jia, Q. *Energy Environ. Sci.* **2016**, *9*, 2418−2432.
(26) Zitolo, A.; Goellner, V.; Armel, V.; Sougrati, M.-T.; Mineva, T.; Stievano, L.; Fonda, E.; Jaouen, F. *Nat. Mater.* **2015**, *14*, 937−942.
(27) Ishihara, A.; Lee, K.; Doi, S.; Mitsushima, S.; Kamiya, N.; Hara, M.; Domen, K.; Fukuda, K.; Ota, K. *Electrochem. Solid-State Lett.* **2005**, *8*, A201−A203.
(28) Vante, N. A.; Tributsch, H. *Nature* **1986**, *323*, 431−432.
(29) Ramaswamy, N.; Allen, R. J.; Mukerjee, S. *J. Phys. Chem. C* **2011**, *115*, 12650−12664.
(30) Stolbov, S. *J. Phys. Chem. C* **2012**, *116*, 7173−7179.
(31) Ziegelbauer, J. M.; Gulla, A. F.; O'Laoire, C.; Urgeghe, C.; Allen, R. J.; Mukerjee, S. *Electrochim. Acta* **2007**, *52*, 6282−6294.
(32) Ramaswamy, N.; Mukerjee, S. *J. Phys. Chem. C* **2011**, *115*, 18015−18026.
(33) Arruda, T. M.; Shyam, B.; Lawton, J. S.; Ramaswamy, N.; Budil, D. E.; Ramaker, D. E.; Mukerjee, S. *J. Phys. Chem. C* **2010**, *114*, 1028−1040.
(34) Jia, Q.; Liang, W.; Bates, M. K.; Mani, P.; Lee, W.; Mukerjee, S. *ACS Nano* **2015**, *9*, 387−400.
(35) Newville, M. *J. Synchrotron Radiat.* **2001**, *8*, 322−324.
(36) Ravel, B.; Gallagher, K. *Phys. Scr.* **2005**, *T115*, 606−608.
(37) Ankudinov, A. L.; Ravel, B.; Rehr, J. J.; Conradson, S. D. *Phys. Rev. B: Condens. Matter Mater. Phys.* **1998**, *58*, 7565−7576.
(38) Jia, Q.; Caldwell, K.; Ziegelbauer, J. M.; Kongkanand, A.; Wagner, F. T.; Mukerjee, S.; Ramaker, D. E. *J. Electrochem. Soc.* **2014**, *161*, F1323−F1329.

DOI: 10.1021/acscatal.6b02417
ACS Catal. 2017, 7, 581−591

(39) Teliska, A.; O'Grady, W. E.; Ramaker, D. E. *J. Phys. Chem. B* **2005**, *109*, 8076−8084.
(40) Ziegelbauer, J. M.; Gatewood, D.; Gulla, A. F.; Guinel, M. J. F.; Ernst, F.; Ramaker, D. E.; Mukerjee, S. *J. Phys. Chem. C* **2009**, *113*, 6955−6968.
(41) Arruda, T. M.; Shyam, B.; Ziegelbauer, J. M.; Mukerjee, S.; Ramaker, D. E. *J. Phys. Chem. C* **2008**, *112*, 18087−18097.
(42) Rao, C. V.; Viswanathan, B. *J. Phys. Chem. C* **2007**, *111*, 16538−16543.
(43) Kelechukwu, B. O.; Israel, O. O.; Emeka, E. O.; Ihebrodike, M. M.; Lebe, N.; Joseph, E. *Int. Lett. Chem., Phys. Astron.* **2013**, *24*, 17.
(44) Zaikovskii, V. I.; Nagabhushana, K. S.; Kriventsov, V. V.; Loponov, K. N.; Cherepanova, S. V.; Kvon, R. I.; Bönnemann, H.; Kochubey, D. I.; Savinova, E. R. *J. Phys. Chem. B* **2006**, *110*, 6881−6890.
(45) Alonso-Vante, N.; Tributsch, H.; Solorza-Feria, O. *Electrochim. Acta* **1995**, *40*, 567−576.
(46) Malakhov, I. V.; Nikitenko, S. G.; Savinova, E. R.; Kochubey, D. I.; Alonso-Vante, N. *J. Phys. Chem. B* **2002**, *106*, 1670−1676.
(47) He, Q. G.; Yang, X. F.; Chen, W.; Mukerjee, S.; Koel, B.; Chen, S. W. *Phys. Chem. Chem. Phys.* **2010**, *12*, 12544−12555.
(48) Park, H.-Y.; Yoo, S. J.; Kim, S. J.; Lee, S.-Y.; Ham, H. C.; Sung, Y.-E.; Kim, S.-K.; Hwang, S. J.; Kim, H.-J.; Cho, E.; et al. *Electrochem. Commun.* **2013**, *27*, 46−49.
(49) He, Q. G.; Shyam, B.; Nishijima, M.; Ramaker, D.; Mukerjee, S. *J. Phys. Chem. C* **2013**, *117*, 4877−4887.
(50) Stampfl, C.; Schwegmann, S.; Over, H.; Scheffler, M.; Ertl, G. *Phys. Rev. Lett.* **1996**, *77*, 3371−3374.
(51) Babu, P. K.; Lewera, A.; Chung, J. H.; Hunger, R.; Jaegermann, W.; Alonso-Vante, N.; Wieckowski, A.; Oldfield, E. *J. Am. Chem. Soc.* **2007**, *129*, 15140−15141.
(52) Norskov, J. K.; Bligaard, T.; Rossmeisl, J.; Christensen, C. H. *Nat. Chem.* **2009**, *1*, 37−46.

DOI: 10.1021/acscatal.6b02417
ACS Catal. 2017, 7, 581−591